

Irreversible Thermodynamics Approach and Modeling of Shear-Banding Flow of Wormlike Micelles

F. Bautista, J. F. A. Soltero, E. R. Macías, and J. E. Puig*

Departamento de Ingeniería Química—CUCEI, Universidad de Guadalajara,
Boul. M. García Barragán No. 1451, Guadalajara, Jal. 44430, Mexico

O. Manero

Instituto de Investigaciones en Materiales, Universidad Nacional Autónoma de México,
Apdo. Postal 70-360, México, D.F. 04510, Mexico

Received: March 6, 2002; In Final Form: August 16, 2002

The flow in a pipe of wormlike micellar solutions is examined using a simple model that consists of the codeformational Maxwell constitutive equation and a kinetic equation that accounts for the breaking and reformation of micelles. The model needs six parameters, *all of which* are extracted from single independent rheological experiments. One of the parameters, the *shear-banding intensity* parameter is associated with the stress plateau in the shear-banding region. The stress plateau is set in our model by the criterion of equal extended Gibbs free energy of the bands. The model predicts a Newtonian (parabolic profile) flow at low-shear rates or low-pressure gradients, followed by shear thinning up to a critical rate where instabilities and long transients appear. At this critical shear rate, a shear-banding flow region arises near the pipe wall. The model indicates that tube lengths up to 400 diameters are required to obtain fully developed flow, where a pluglike profile at the center of the tube coexists with a region supporting a much higher shear rate next to the wall. Shear-banding flow is present up to a second critical shear rate. At shear rates larger than the second critical rate, the parabolic velocity profile is recovered, except near the center of the tube where a small shear-banding flow region remains because the stress at that radial position is equal to the plateau stress. This is a consequence of the linear dependence of the shear stress with the pipe radius. The predictions of the model are compared with experimental results from the literature.

Introduction

The rheological behavior of wormlike micelles is rich and varied because they can form entanglements in the semidilute regime akin to polymer solutions, and because they break and reform continuously.^{1–14} In the linear viscoelastic regime, the rheological response of wormlike micelles at low frequencies spans from near Maxwell behavior with a single relaxation time to polymer-like behavior with a stretch exponential spectra of relaxation times, depending on the ratio of the breaking τ_{break} and the reptation τ_{rep} times.^{15–19} In the fast breaking regime ($\tau_{\text{break}}/\tau_{\text{rep}} \ll 1$), the rheological response of micellar solutions at low frequencies tends to Maxwell behavior with a single relaxation time, $\tau_d = (\tau_{\text{break}}\tau_{\text{rep}})^{1/2}$.^{2,4–9,13,15–19}

In the nonlinear viscoelastic regime, at least four regimes have been reported in steady shear experiments as a function of applied shear rate.^{20–25} At low shear rates, a Newtonian region is observed, followed by a shear-thinning region. However, at a critical shear rate, $\dot{\gamma}_{c1}$, a stress plateau, σ_{plateau} , accompanied by oscillations and long transients, is observed. At this rate and up to a second critical shear rate, $\dot{\gamma}_{c2}$, two spatially distinct regions of low and high shear rate coexist. The discontinuity in the $\sigma - \dot{\gamma}$ relationship is due to the spurt effect, also known as *shear-banding flow*.²⁶ Shear-banding flow has been observed by NMR velocimetry,^{23–25} by optical methods,^{27,28} and by small

angle neutron scattering.^{29,30} Above $\dot{\gamma}_{c2}$, the flow becomes homogeneous again and a Newtonian behavior is observed with a smaller shear viscosity. This high-shear-rate branch is hard to detect in cone-and-plate rheometry because flow instabilities expel the sample from the instrument; however, the high-shear-rate branch was conclusively visualized recently in pipe flow by NMR velocimetry.²⁵

To explain shear-banding flow of wormlike micellar solutions, several models have been forwarded. The extension of the reptation-reaction model to the nonlinear rheology of wormlike micellar solutions predicts a stress plateau equal to $0.67G_0$ at a critical shear rate of $2.6/\tau_d$.²⁰ Using the generalized Maxwell equation and a damping function to account for the nonlinear behavior, Callaghan et al. predicted the existence of a maximum in the $\sigma - \dot{\gamma}$ relationship followed by a negative slope regime.²³ However, neither of these models are able to predict the upturn at higher shear rates. Spenley et al., using the Lagrangian–Eulerian method of fluid dynamics combined with the Ottinger’s stochastic method for the constitutive equation, showed that above the critical shear rate, the steady state consists of bands supporting different shear rates.³¹ Others have solved the homogeneous flow equation in several geometries with sophisticated hydrodynamic flow solvers and found a selected stress for shear banding.^{32,33} Also, elastic flow instabilities^{34,35} and secondary flow^{36,37} have been suggested to explain the spurt effect. However, all these approaches consider that shear-banding flow is caused by mechanical flow instabilities.

* To whom correspondence should be addressed. E-mail: puigje@mail.udg.mx or puig_jorge@hotmail.com.

On the other hand, several groups have proposed that shear banding is more akin to a first-order dynamic phase transition—even at concentrations far from *true* phase boundaries, in which mechanical instabilities may or may not play a role.^{29,38–44} Evidence supporting this point of view include (i) robustness of the stress plateau, (ii) slow sigmoidal onset kinetics which is characteristic of nucleation and growth processes of the fluid-oriented phase, and (iii) the similarity of the stress-shear rate curves with the pressure–density isotherms for liquid–gas systems, where nonequilibrium phases may be separated by hypersurfaces (in a field variable space) representing continuous (e.g., critical points or lines) or discontinuous (first-order) transitions.^{41,43} In fact, the existence of “critical” conditions of surfactant concentration and temperature where the stress plateau reduces to one flat inflection point has been observed and “master dynamic phase diagrams” have been constructed.^{41–44}

A simple, although phenomenological, model consisting of the codeformational Maxwell constitutive equation coupled to a kinetic equation for the breaking and reformation of micelles was proposed by us to account for the non linear rheological behavior of wormlike micellar solutions of cetyltrimethylammonium tosylate (CTAT).²² Later, we extended this model to describe the shear-banding behavior of CTAT micellar solutions detected in cone-and-plate rheometry as well as the long transients and oscillations associated with this flow.¹⁴

In this paper, the flow in a pipe of wormlike micellar solutions is examined with our model. First, we compare experimental steady shear results for CTAT micellar solutions obtained by cone-and-plate rheometry²² with the predictions of the model without fitting parameters. The position of the stress plateau in the shear-banding region is determined using irreversible thermodynamics arguments. Then we examine the sensitivity of the various parameters of the model and compare its predictions with recent results reported in the literature for the pipe flow of viscoelastic micellar solutions.

The Model

The model consists of the codeformational Maxwell constitutive equation coupled to a kinetic equation to account for the breaking and reformation of micelles.¹⁴ For simple shear flow, the model reduces to the following system of ordinary differential equations:

$$\sigma_{12} + \frac{1}{G_0\varphi} \frac{d\sigma_{12}}{dt} - \frac{1}{G_0\varphi} \dot{\gamma}_{12} \sigma_{22} = \frac{\dot{\gamma}_{12}}{\varphi} \quad (1)$$

$$\sigma_{ii} + \frac{1}{G_0\varphi} \frac{d\sigma_{ii}}{dt} = \Theta_{ii} \quad (i = 1, 2, 3) \quad (2)$$

$$\frac{d\varphi}{dt} = \frac{(\varphi_0 - \varphi)}{\lambda} + k_0(1 + \mu_1 \dot{\gamma}_{12})(\varphi_\infty - \varphi) \sigma_{12} \dot{\gamma}_{12} \quad (3)$$

Here σ_{12} is the shear stress; $\dot{\gamma}_{12}$ is the shear rate, σ_{ii} ($i = 1, 2$, and 3) are the normal stresses; φ ($\equiv \eta^{-1}$) is the fluidity; η is the shear viscosity, φ_0 and φ_∞ are the fluidities at zero- and at infinite-shear rate; G_0 is the elastic plateau modulus, λ is a structure relaxation time; k_0 is a kinetic constant for structure breakdown, μ_1 can be interpreted as a *shear-banding intensity* parameter; and $\Theta_{ii} = (2\dot{\gamma}\sigma_{12})/(G_0\varphi)$ for $i = 1$, and $\Theta_{ii} = 0$ for $i = 2$ and 3 in eq 2. Because σ_{22} is negligible for CTAT micellar solutions,²² the third term on the left-hand side of eq 1 will be eliminated for the rest of the paper.

For steady simple-shear flow, eqs 1–3 with their time derivatives set to zero give

$$N_1 = \frac{2\sigma_{12} \dot{\gamma}_{12}}{\varphi G_0} \quad (4)$$

$$\varphi^2 - \varphi_0\varphi - k_0\lambda(\varphi_\infty - \varphi)\dot{\gamma}_{12}^2(1 + \mu_1\dot{\gamma}_{12}) = 0 \quad (5)$$

where N_1 ($\equiv \sigma_{11} - \sigma_{22}$) is the first normal stress difference. Consider now the fully developed isothermal flow of an incompressible fluid in a tube of radius R and length L where the pressure drop along the length of the tube is ΔP . For this situation, the shear stress distribution is given by

$$\sigma_{12} = \frac{r}{2} \frac{\Delta P}{L} \quad (6)$$

The shear stress at the tube wall is then given by eq 6 with $r = R$. Usually in flow in a tube, the volumetric flow rate Q is measured. The volumetric flow rate can be calculated from fluidity data as

$$Q = \pi \Delta P \int_0^R r' \left\{ \int_0^{r'} \xi \varphi(\xi) d\xi \right\} dr' \quad (7)$$

The model needs six parameters to predict experimental data: φ_0 , φ_∞ , G_0 , k_0 , λ , and μ_1 . All of them can be estimated from rheological experiments as described below. φ_0 is the inverse of the zero-shear rate Newtonian viscosity in steady shear experiments. φ_∞ can be obtained from the high-shear-rate plateau in steady shear measurements. However, the range of shear rates needed to determine φ_∞ usually cannot be reached in cone-and-plate rheometry; hence, φ_∞ can be obtained by fitting the viscous modulus G'' with the Hess model, given by

$$G'' = \left(\frac{\eta_0 - \eta_\infty}{\tau_d} \right) \left(\frac{\omega \tau_d}{1 + \omega^2 \tau_d^2} \right) + \omega \eta_\infty \quad (8)$$

⁴⁵ where τ_d is the main relaxation time of the sample and ω is the applied frequency.

G_0 can be obtained by oscillatory shear measurements or from instantaneous stress relaxation experiments. The agreement between the values of G_0 obtained from these two experiments is within 10%.¹³ The structural relaxation time λ can be estimated from the intercept of the stress relaxation curve at long times after cessation of steady shear flow, where the intercept is given by $\exp[-G_0\lambda(\varphi_{ss} - \varphi_0)]$, φ_{ss} being the steady-state fluidity prior to the cessation of shear flow.⁴⁶ The parameter k_0 , in turn, can be evaluated by fitting numerically the stress growth coefficient η^+ from inception of shear flow experiments.⁴⁶ The *shear-banding intensity* parameter μ_1 , as it will be discussed below, is uniquely determined by the value of the stress at the plateau region.

Figure 1 depicts the values of the experimentally measured parameters at 25 °C for CTAT micellar solutions. The solid lines are only aids to the eye. The plateau elastic modulus G_0 follows a power law dependence on surfactant concentration with an exponent equal to 2.0. Similar dependence has been reported elsewhere.^{47,48}

Irreversible Thermodynamics Flow Analysis

According to the extended irreversible thermodynamics of viscoelastic fluids under flow, the generalized Gibbs

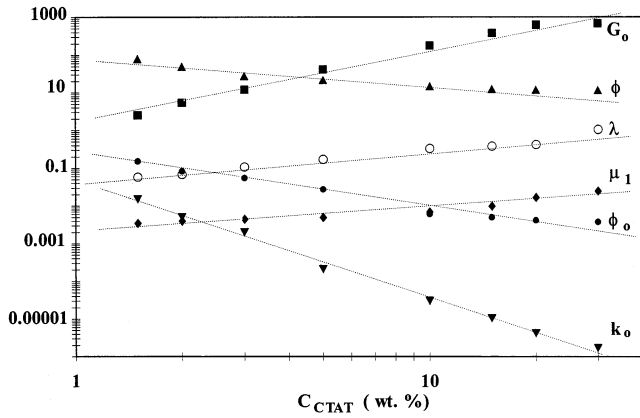


Figure 1. Experimental values of the parameters of the model determined at 30 °C as a function of CTAT concentration: (■) G_0 , (▲) φ_∞ , (●) φ_0 , (○) λ , (▼) k_0 , (◆) μ_1 .

equation is given by⁴⁹

$$ds = T^{-1}du + T^{-1}Pdv - T^{-1}\left(\frac{v\tau\varphi}{2}\right)\sigma:d\sigma \quad (9)$$

Here s is the extended specific entropy, T the absolute temperature, u the specific internal energy, P the thermodynamic pressure, v the specific volume, τ the stress relaxation time, and σ the stress tensor.

For simple shear flow, only the shear stress σ_{12} and the normal stress components σ_{ii} ($i = 1, 2$, and 3) remain. Hence, after performing the double-dot tensor product indicated in eq 9 and using the definition of the extended Gibbs free energy $G (\equiv u - Ts + Pv)$ to get rid of the extended entropy, one obtains

$$dG = -sdT - vdP + \left(\frac{v\tau\varphi}{2}\right)(2\sigma_{12}d\sigma_{12} + \sum_{i=1}^3 \sigma_{ii}d\sigma_{ii}) \quad (10)$$

In steady simple shear flow, eqs 1 and 3 yield a cubic equation in shear rate [eq 5]. Also, in steady state, $\sigma_{11} = (2\dot{\gamma}\sigma_{12})/(G_0\varphi)$ [eq 2 with $i = 1$] and $\sigma_{22} = \sigma_{33} = 0$ [eq 2 with $i = 2$ and 3], and since $\sigma_{12} = \dot{\gamma}/\varphi$ from eq 1, then $\sigma_{11} = 2\sigma_{12}^2/G_0$. Hence, the extended Gibbs free energy for simple shear flow (eq 10) under *isobaric* and *isothermal* conditions becomes

$$dG = (v\tau\varphi)\left(\frac{4\sigma_{12}^3}{G_0^2} + \sigma_{12}\right)d\sigma_{12} \quad (11)$$

In terms of shear rate, eq 11 can be written, using eq 5, as

$$dG = v\tau\left(\frac{4\sigma_{12}^3}{G_0^2} + \sigma_{12}\right)(1 - \beta)d\dot{\gamma}_{12} \quad (12)$$

where

$$\beta = \frac{k_0\lambda(\varphi_\infty - \varphi)(2 + 3\mu_1\dot{\gamma})}{\varphi^2 + k_0\lambda\dot{\gamma}^2\varphi_\infty(1 + \mu_1\dot{\gamma})}$$

It can be easily shown that $\beta \rightarrow 0$ as $\dot{\gamma} \rightarrow \dot{\gamma}_\infty$, and because the range of the parameters of the model given in Figure 1, β is small as $\dot{\gamma} \rightarrow 0$. Hence, eq 12 can be approximated to

$$dG = v\tau\left(\frac{4\sigma_{12}^3}{G_0^2} + \sigma_{12}\right)d\dot{\gamma}_{12} = \frac{v}{G_0\varphi_0}\left(\frac{4\sigma_{12}^3}{G_0^2} + \sigma_{12}\right)d\dot{\gamma}_{12} \quad (13)$$

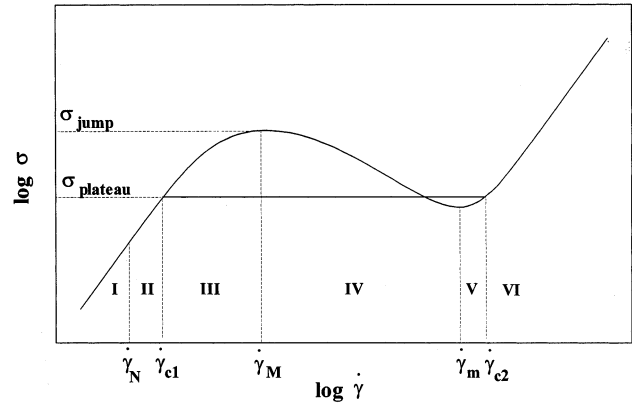


Figure 2. Schematic representation of the shear stress versus shear rate relationship for fluids that exhibit the spurt effect.

In eq 13, $\tau[\equiv(G_0\varphi_0)^{-1}]$ is the Maxwell relaxation time. In strict sense, τ is a function of the fluidity φ and hence it is not a constant. However, as a first approximation, small departures from φ_0 are considered here. Within this approximation, normal stresses can be neglected, and eq 13 reduces to

$$dG = \left(\frac{v}{G_0\varphi_0}\right)\sigma_{12}d\dot{\gamma}_{12} \quad (14)$$

Substitution of the steady-state version of eq 1 in eq 14 and integration gives

$$\Delta G = \left(\frac{v}{G_0\varphi_0}\right) \int \frac{\dot{\gamma}_{12}}{\varphi} d\dot{\gamma}_{12} \quad (15)$$

where φ is the solution of eq 5.

Inasmuch as the working equations are written in terms of the shear stress and the shear rate, subscripts in these two variables will be dropped in the rest of the paper for simplicity.

Results

A schematic nonmonotonic representation of the σ - $\dot{\gamma}$ relationship, first suggested by McLeish and Ball⁵⁰ to explain the spurt effect in polymer solutions, is portrayed in Figure 2. For shear rates below $\dot{\gamma}_N$, a Newtonian behavior is followed with $\eta = \eta_0$ (region I). Shear thinning behavior is observed above $\dot{\gamma}_N$ (region II) up to $\dot{\gamma}_{cl}$, at which the shear rate becomes multivalued and a stress plateau appears. However, under some circumstances, a metastable branch has been detected (region III) up to a critical stress, known as *top jumping stress*.²¹ For larger stresses, the system becomes unstable since $(d\sigma/d\dot{\gamma})_{P,T} < 0$ ⁴⁴ and, as a consequence, shear banding develops (region IV). In this region, as mentioned before, bands supporting different shear rates coexist. Once the second critical shear rate $\dot{\gamma}_{c2}$ is exceeded, a homogeneous Newtonian forms again (region VI) but with a smaller viscosity (η_∞). A second metastable branch may occur at high shear rates (region V). Britton et al. discovered recently this branch in pipe flow experiments performed in a decreasing shear-rate mode.²⁵

The steady relationship between σ and $\dot{\gamma}$, as predicted with eq 5, is depicted in Figure 3, using values for parameters typical of CTAT micellar solutions (Figure 1). The predicted curve has the sigmoid shape shown in Figure 2. According to eq 15, the extended Gibbs free energy versus $\dot{\gamma}$ curve exhibits one or two minima, depending whether the shear rate (or the stress) lies outside or inside the multi-valued region. For shear stresses smaller than σ_b or larger than σ_d , there is a one-to-one correspondence between the shear stress and the shear rate. The

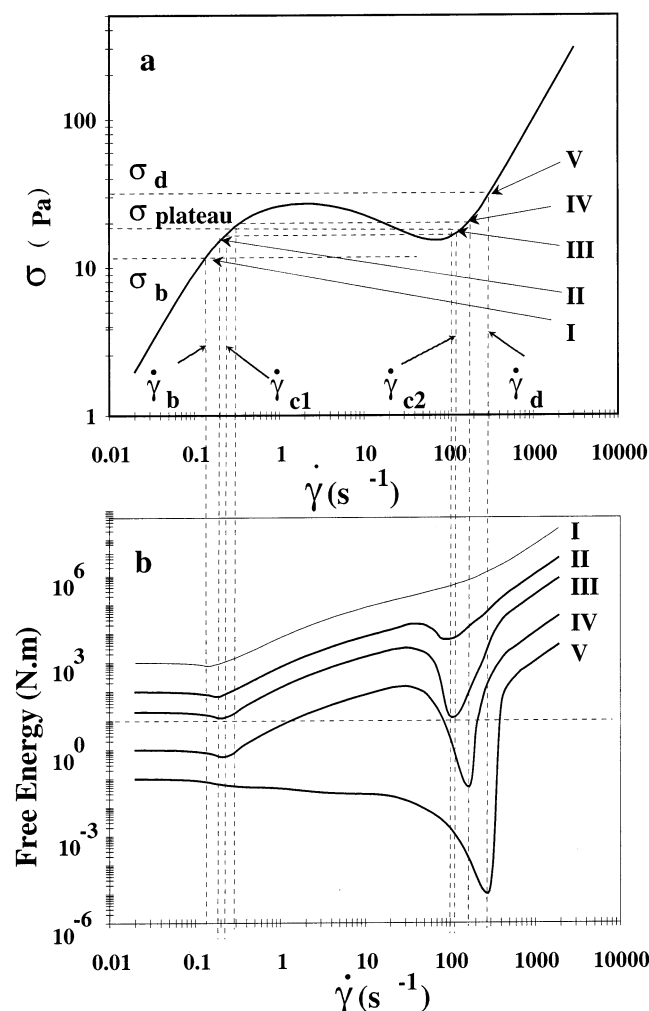


Figure 3. (a) Shear stress versus shear rate plot, where the location of the plateau stress, the span of the multivalued region, the metastable region and the homogeneous flow region are indicated. (b) Extended Gibbs free energy plotted versus the shear rate for various applied stresses. The actual values of the stresses have been multiplied by constant factors: I ($12.5 \text{ Pa} \times 4000$); II ($15.25 \text{ Pa} \times 100$); III ($15.865 \text{ Pa} \times 20$); IV ($18.9 \text{ Pa} \times 1$); and V ($21 \text{ Pa} \times 0.1$) for better observation of the curves.

extended Gibbs free energy exhibits a single absolute minimum at each applied shear rate in these two homogeneous regions (see curves I and V in Figure 3b). However, for shear stresses between σ_b and σ_d , the relationship between σ and $\dot{\gamma}$ becomes multi-valued and so, the extended free energy exhibits two minima. A very important result is the fact that equal extended free energy minima occur only when the shear rates are $\dot{\gamma}_{c1}$ and $\dot{\gamma}_{c2}$ (Figure 3b). Consequently, the stress plateau ($\sigma_{plateau}$) and the critical shear rates ($\dot{\gamma}_{c1}$ and $\dot{\gamma}_{c2}$) for shear banding can be uniquely determined. On the other hand, when the stress is larger than σ_b but smaller than $\sigma_{plateau}$, the extended Gibbs free energy curve also exhibits two minima of different depth at the low- and the high- shear-rate sides of the sigmoid (curve II in Figure 3b). The lowest minimum corresponds to the low-shear-rate side, which indicates that the flow is homogeneous and that the fluid is supporting only the low shear rate. However, when the stress is larger than $\sigma_{plateau}$ but smaller than σ_d (i.e., within the metastable branch), the extended Gibbs free energy shows two minima, where the deeper minimum appears at the high-shear-rate side (curve IV in Figure 3b). This implies that the more stable state is the high-shear-rate side. Hence, under these circumstances, the flow is also homogeneous and the fluid is now supporting only the high shear rate. In summary, there

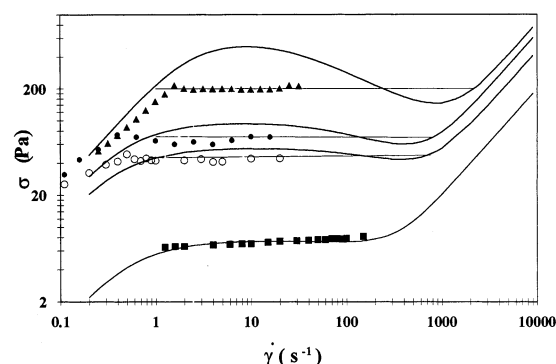


Figure 4. Shear stress versus shear rate measured in cone-and-plate rheometry at 30 °C for micellar solutions of CTAT: (■) 2 wt %, (○) 5 wt %, (●) 10 wt %, (▲) 20 wt %. Solid lines are the predictions of the model. Lines joining the low- and high-shear-rate branches of the sigmoid in the shear-banding region (coexistence line) were set according to the criterion of equal Gibbs free energy of fluid bands supporting the low and the high shear rates (eq 20).

is heterogeneous flow between $\dot{\gamma}_{c1}$ and $\dot{\gamma}_{c2}$, and homogeneous flow below $\dot{\gamma}_{c1}$ and above $\dot{\gamma}_{c2}$.

The existence of the metastable branches can also be understood in terms of the analysis presented here. The calculations shown in Figure 3 indicate that local free energy minimum exists at both branches. Hence, if either of these branches is reached by, for example, controlled-stress measurements, the local free energy minimum guarantees its existence until large enough fluctuations shift the system to the overall minimum within the shear-banding region and, as a consequence, two bands will form, whose proportions are determined by the lever rule,^{41,44,51} i.e.,

$$\dot{\gamma} = x_1 \dot{\gamma}_{c1} + (1 - x_1) \dot{\gamma}_{c2} \quad (16)$$

Figure 4 shows the experimental shear stress as a function of shear rate measured with cone-and-plate geometry for CTAT micellar solutions of various concentrations. The solid lines represent the predictions of our model using the parameters reported in Figure 1. As described above, at moderate and high CTAT concentrations, our model predicts a sigmoid similar to that shown in Figure 2. This sigmoid fade as the CTAT concentration diminishes. In fact, our model predicts a monotonic increasing relationship between σ and $\dot{\gamma}$ with a near-zero slope that follows closely the experimental data for the 2 wt % CTAT solution, which has a very small μ_1 value (Figure 1). As discussed elsewhere,¹⁴ this result is due to both the decreasing value of the product of k_0 and λ^{22} and to the decrease in the shear-banding intensity parameter (Figure 1; also Figure 2 of ref 14), with diminishing CTAT concentration. Inasmuch as $k_0\lambda$ and μ_1 are cofactors of $\dot{\gamma}^3$ in eq 5, the quadratic term begins to dominate as these parameters become smaller and so, the sigmoid tends to wash out. On the other hand, for higher CTAT concentrations, our model reveals a sigmoid whereas the experimental data depict a stress plateau. Nevertheless, the dividing line that joints the critical shear rates $\dot{\gamma}_{c1}$ and $\dot{\gamma}_{c2}$ passes through the experimental data. As described above, the criterion employed to set the position of the stress plateau is that the bands at the critical shear rates should have equal extended Gibbs free energies. This criterion sets the value of the shear-banding intensity parameter and yields a *unique* relationship between $\sigma_{plateau}$ and μ_1 .

Figure 5 illustrates how the σ – $\dot{\gamma}$ relationship (Figure 5a) is related to the pressure drop along the tube radius (Figure 5b), to the extended Gibbs free energy as a function of shear rate

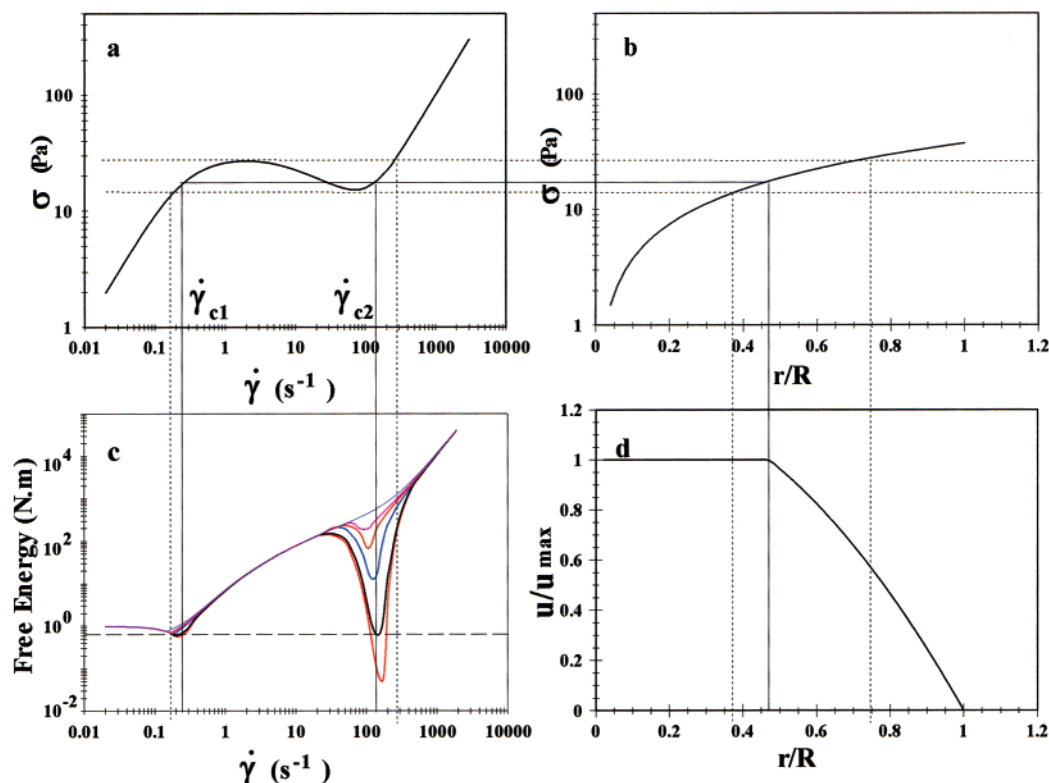


Figure 5. Schematic representation of the relationship between the nonmonotonic constitutive equation between shear stress and shear rate (a), the wall-shear stress as a function of tube radial position (b), the extended Gibbs free energy, calculated from irreversible thermodynamics, as a function of shear rate (c), and the velocity profile in the steady flow in the pipe (d).

(Figure 5c), and to the velocity profile (Figure 5d). When the shear rate is smaller than $\dot{\gamma}_{c1}$, the parabolic profile typical of the Poiseuille flow of a Newtonian fluid is observed. In fact, the model forecasts a parabolic velocity profile with a power-law exponent n close to 1. However, the stress varies linearly with radius in pipe flow. So, when the stress at the tube wall becomes equal to the plateau stress, the model predicts two bands: one in the core supporting a lower shear rate, $\dot{\gamma}_{c1}$, and another next to the wall supporting a higher shear rate, $\dot{\gamma}_{c2}$. The plateau stress value set by the equal-extended Gibbs free energy criterion leads to two stable branches in the low- and high-shear-rate regions, respectively (Figure 5c). The plateau stress line in Figure 5a corresponds to a single point in Figure 5b and, hence, to a boundary between the two bands in the velocity profiles shown in Figure 5d. However, if we allow for an unsteady-state situation along the metastable branch (*stress top jumping*), the flow is likely to become unstable. This is observed in the section of the velocity profile corresponding to the area located between the top jumping and the minimum in Figure 5a. Nevertheless, the analysis by Irreversible Thermodynamics of the metastable and unstable regions indicates that only that shear rate which gives the minimum in extended Gibbs free energy (Figure 5c) yields the right velocity profile, even though there are three values of shear rate (Figure 5a). The same analysis also demonstrates that the equal-free energy criterion that fixes *uniquely* μ_1 corresponds to the equal minimum values of the extended Gibbs free energy at $\dot{\gamma}_{c1}$ and $\dot{\gamma}_{c2}$ (Figure 5c). For shear rates higher than $\dot{\gamma}_{c2}$, a Newtonian velocity profile is recovered again but with a smaller viscosity, although a small shear-banding flow region remains near the tube center.

Figure 6 shows the effect of the shear-intensity parameter μ_1 on the flow behavior in a tube at a fixed pressure gradient (i.e., fixed wall-shear stress). The values of the other parameters of the model are similar to those for CTAT micellar solutions

(Figure 1). Elsewhere we showed that the stress plateau becomes wider as μ_1 increases.¹⁴ Also, σ_{plateau} , $\dot{\gamma}_{c1}$, and $\dot{\gamma}_{c2}$ shift to lower values as the shear intensity parameter rises (inset in Figure 6) until it reaches a limiting value at high μ_1 . In flow in a tube, neither shear banding nor instabilities are predicted when $\mu_1 = 0$. Instead, a smooth velocity profile typical of a shear thinning fluid develops with a power law exponent, $n = 0.98$ (black profile in Figure 6). However, for values of μ_1 greater than zero, a band near the tube wall supporting a higher shear rate is predicted (red and blue profiles in Figure 6). The thickness of this band increases as the shear-banding intensity parameter increases since the critical shear stress and the critical shear rate shift to smaller values.

Figure 7 depicts velocity profiles as a function of the wall stress σ_w . To isolate the effect of this variable, the value of μ_1 is set equal to 0.1 and the other parameters are the same as those used in Figure 6. When the wall-shear rate is smaller than $\dot{\gamma}_N$, the parabolic profile of a Newtonian fluid is predicted (black profile in Figure 7). When the applied stress gives $\dot{\gamma}$ -values between $\dot{\gamma}_N$ and $\dot{\gamma}_{c1}$, the profile is no longer Newtonian but that of a shear-thinning fluid (green profile in Figure 7). However, when the applied stress (i.e., pressure gradient) becomes equal to or slightly larger than the stress plateau value, a band supporting a higher shear rate appears near the tube wall with a rapid rise in shear stress at the wall (blue profile in Figure 7). This band coexists with another one supporting a smaller shear rate at the center of the tube. On the other hand, when the applied stress is at the high-shear-rate branch of the σ - $\dot{\gamma}$ flow curve (see Figure 2), the Newtonian parabolic profile is recovered but a small shear-banding region remains in the pipe center (red profile in the inset of Figure 7).

Figure 8 reports experimental and predicted wall-shear stress versus apparent shear rate, $\dot{\gamma}_{\text{app}} [=4Q/(\pi R^3)]$ for a 2 wt % CTAT solution as a function of L/D . Experimental data, measured in

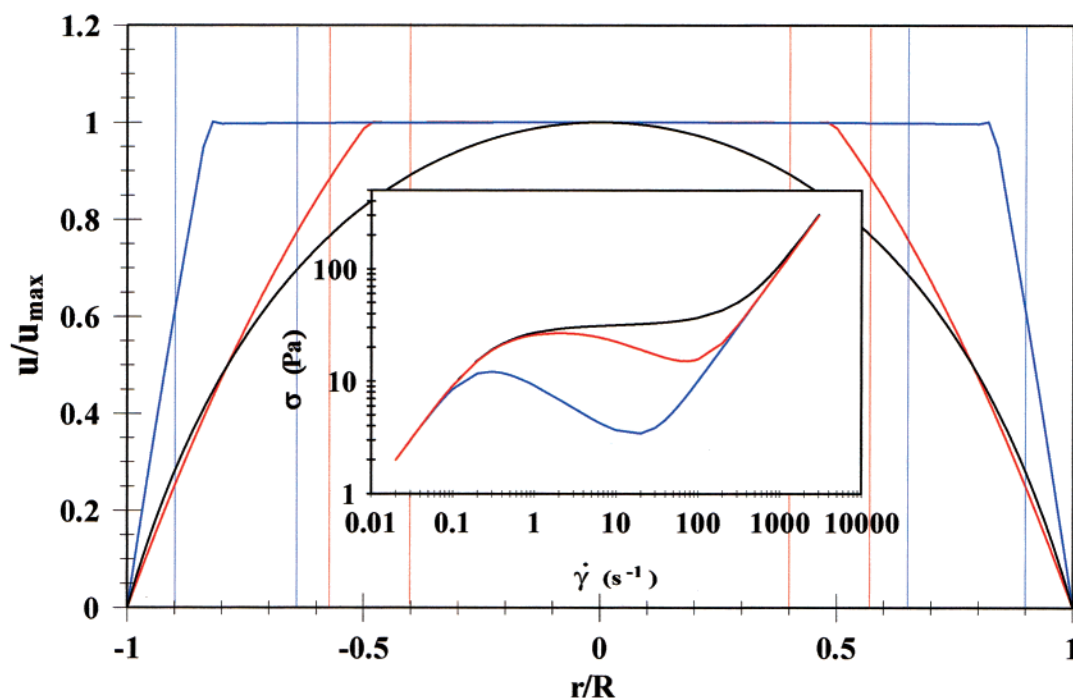


Figure 6. Normalized axial velocity as a function of normalized radial position for different values of the shear-banding intensity parameter μ_1 in s : 0 (black line), 1 (red line), and 10 (blue line) and $\nabla P = 200$ Pa/m. Values of the other parameters are $\varphi_0 = 0.01$ Pa $^{-1}$ s $^{-1}$, $\varphi_\infty = 10$ Pa $^{-1}$ s $^{-1}$. $G_0 = 100$ Pa and $k_0\lambda = 10^{-4}$ Pa $^{-1}$ s. Inset: Shear stress versus shear rate curve for data shown in figure.

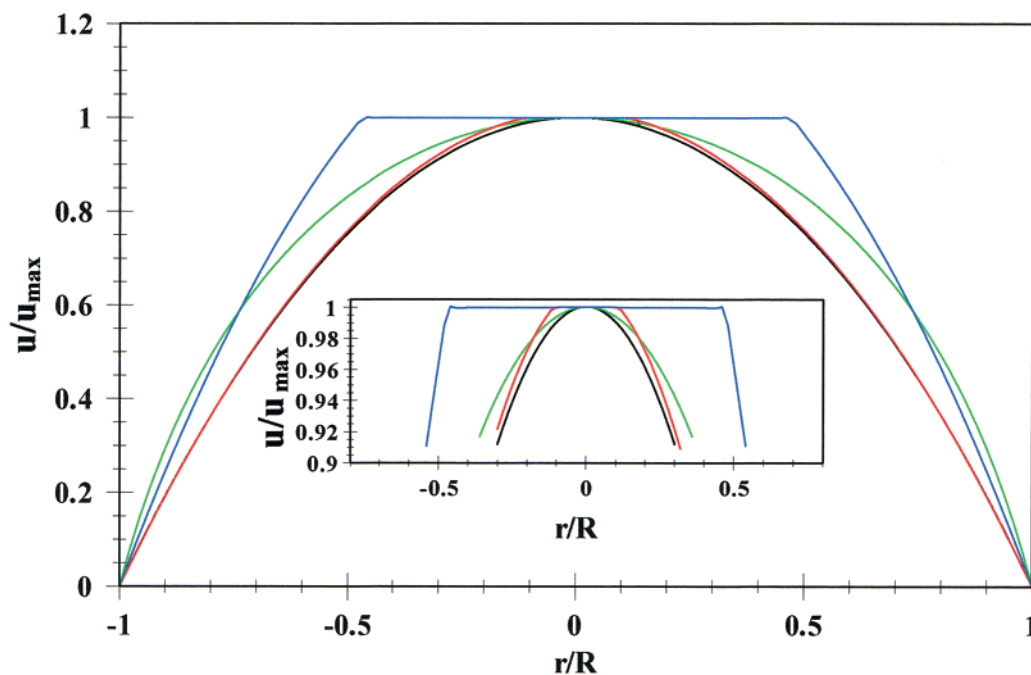


Figure 7. Normalized axial velocity as a function of normalized radial position for different pressure gradients in Pa/m: 50 (black line), 200 (green line), 600 (blue line), 800 (red line). The critical pressure gradient for shear banding is 300 Pa/m. The parameters employed in the calculations are the same than those used in Figure 5 but with $\mu_1 = 0.1$ s. Inset: Scaleup of the profiles near the center of the tube.

a capillary tube of 3 mm in diameter, were taken from Hernández-Acosta et al.⁵² Steady shear data were measured in a Rheometrics RSD-II mechanical spectrometer in a cone-and-plate geometry (diameter of 5 cm and angle of 2.28°).²² For shear rates larger than the critical value, hundredths main relaxation times of the sample were required to reach steady conditions in cone-and-plate measurements.²² Pipe-flow data for $L/D = 400$ coincide with the cone-and-plate data. Also, notice that data for $L/D = 50$ and 100 superimpose with that for $L/D = 400$ up to shear rates around 10 s $^{-1}$, i.e., for shear rates smaller than $\dot{\gamma}_{cl}$. For shear rates larger than this critical value, data for

$L/D = 50$ lie above those for $L/D = 100$ and both are above the data obtained for $L/D = 400$. Results reported elsewhere⁵² emphasize the importance of the residence time of the fluid in pipe flow. Notice also that the predictions of our model for $L/D = 400$ superimpose the experimental pipe flow data for the same L/D ratio and the cone-and-plate steady data. However, the model slightly overpredicts data for smaller L/D ratios, although the predictions follow the same tendencies as those of the experimental data: that is, departures from steady-state conditions become larger as L/D diminishes. For very small lengths, our predictions show that the plot of σ_w versus $\dot{\gamma}_{app}$ becomes a

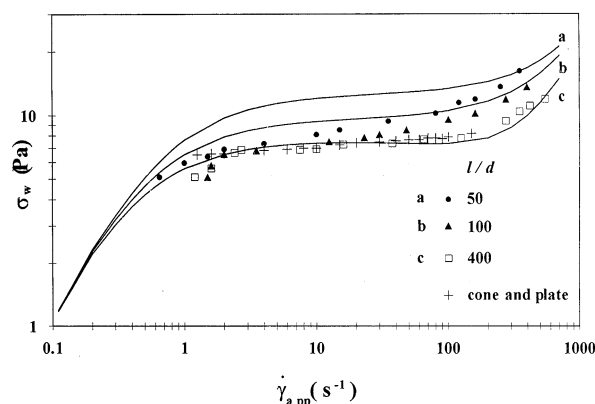


Figure 8. Wall shear stress versus apparent shear rate for the flow of a 2 wt % CTAT micellar solution for different L/D values. Symbols are experimental values taken from ref 40 and solid lines are the predictions of the model for different L/D values. Also for comparison, steady values (+) obtained by cone-and-plate rheometry are included.

straight line (not shown), indicating a Newtonian behavior, which means that the shear-banding flow has not had enough time to develop.

Velocity profiles as a function of a dimensionless flow time, t/τ_d , are shown in Figure 9 for applied pressure gradients such that the wall-shear rate is below $\dot{\gamma}_{c1}$, between $\dot{\gamma}_{c1}$ and $\dot{\gamma}_{c2}$ (i.e., within the shear-banding region), or above $\dot{\gamma}_{c2}$ (i.e., in the high-shear-rate branch of the σ – $\dot{\gamma}$ flow curve). When the applied gradient produces wall-shear rates smaller than $\dot{\gamma}_N$, the velocity profile develops very rapidly, i.e., within fractions of the main relaxation time of the sample. After a few L/D , the parabolic profile, typical of Poiseuille flow, forms (Figure 9a). At higher shear rates but still lower than the first critical shear rate for spurt flow, the approach to fully developed flow is fast but now the profile of a shear thinning fluid is observed (not shown). This profile can be fitted accurately with the power law constitutive equation with an exponent n between 0 and 1, depending on the level of the applied shear rate. As the wall-shear rate approaches $\dot{\gamma}_{c1}$, the time required for achieving fully developed flow increases; also deviations from the parabolic profile are noticed. Figure 9b shows velocity profiles as a function of time for shear rates larger than $\dot{\gamma}_{c1}$ but smaller than $\dot{\gamma}_{c2}$. For this situation, our model predicts that tube lengths longer than 200 diameters ($L/D > 200$) are needed to reach the fully developed flow condition. Moreover, fluctuations are seen even for $L/D > 400$, that is, for very long residence times. At short times, the profile is parabolic, evolving into a flat profile at long times (inset in Figure 9). A larger viscosity (η_0) of the fluid in the central region is predicted, coexisting with a region supporting a much larger shear rate near the tube wall, where $\eta \approx \eta_\infty$ ($\eta_0/\eta_\infty \geq 1000$). When the second critical shear rate, $\dot{\gamma}_{c2}$, is exceeded, that is, for very high volumetric flow rates, fully developed flow is again accomplished very rapidly and the parabolic profile is recovered, although a small shear-banding flow region remains in the pipe center (Figure 9c). As described before (Figure 5), this is a consequence of the linear dependence of the shear stress (or shear rate) on the pipe radial position that causes a small portion of the fluid to be at the shear-banding flow region whenever the wall-shear rate becomes larger than $\dot{\gamma}_{c2}$.

To stress the importance of the residence time in achieving totally developed shear-banding flow, the ratio between the time required to reach steady-state conditions and the main relaxation time of the sample t_{ss}/τ_d is depicted in Figure 10 as a function of the pressure gradient ∇P . When the applied pressure gradient is below the critical value for shear banding ($\nabla P_{crit} = 300$ Pa/m for the case shown in Figure 10), steady state is achieved very

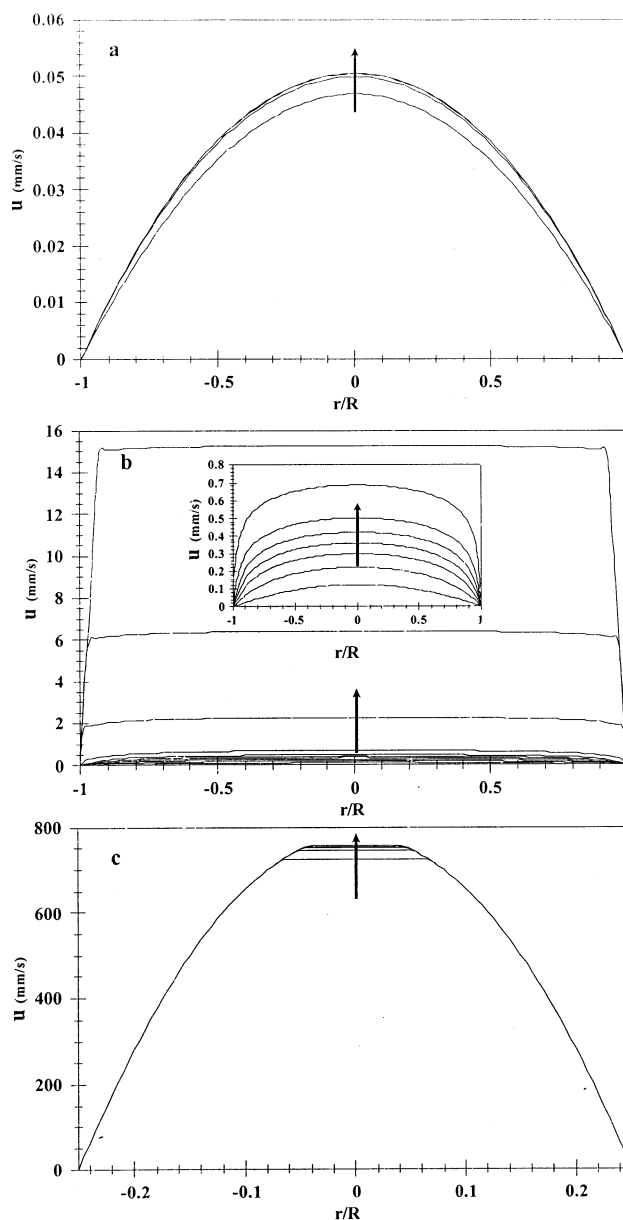


Figure 9. Velocity profiles as a function of residence time for three different pressure gradients: (a) 40 Pa/m, (b) 320 Pa/m, (c) 800 Pa/m. The critical pressure gradient for shear banding for this flow situation is 300 Pa/m. The values of the parameters employed are the same as those used in Figure 6 with μ_1 in 0.1 s. Arrows indicate the time evolution of the profiles.

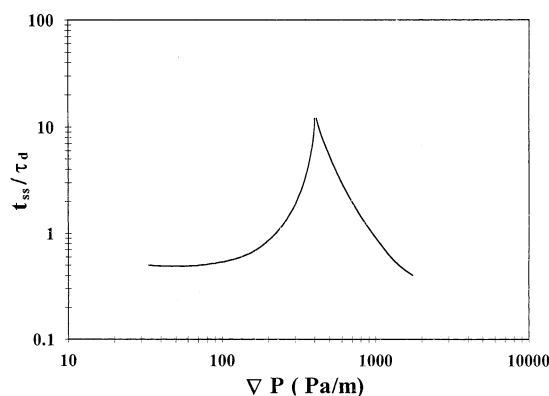


Figure 10. Ratio of time to reach steady state to main relaxation time t_{ss}/τ_d versus applied pressure gradient in pipe flow of micellar solutions. The parameters used are the same as those in Figure 6 with μ_1 in 0.1 s.

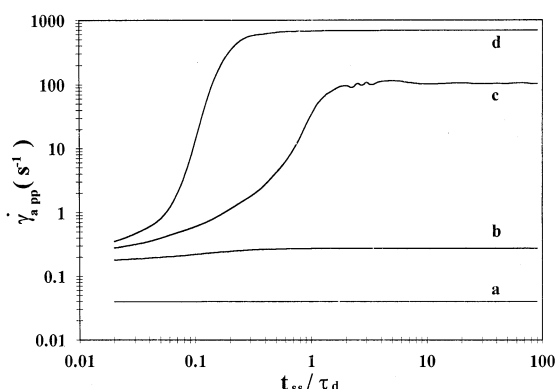


Figure 11. Apparent shear rate versus dimensionless time for different applied pressure gradients: (a) 10 Pa/m, (b) 40 Pa/m, (c) 320 Pa/m, (d) 800 Pa/m. The critical pressure gradient for shear banding for this flow situation is 300 Pa/m. The parameters employed are the same as those in Figure 6 with $\mu_1 = 0.1$ s.

rapidly, within fractions of the main relaxation time of the sample. However, once ∇P reaches values at which shear banding begins to develop, the time required to arrive to the steady-state conditions increases rapidly, reaching hundredths relaxation times. Moreover, there is a ∇P range where no steady state is ever reached. Such long transients have been observed when shear-banding flow occurs in cone-and-plate measurements^{21,22} and recently uncovered by Hernandez-Acosta et al. in pipe flow of wormlike CTAT micellar solutions.⁵² When the high-shear-rate branch is approached, our model predicts that the steady state is reached again quite rapidly. Incidentally, the plot shown in Figure 10 resembles that of t_{ss}/τ_d versus $\dot{\gamma}$ observed experimentally and predicted by our model for cone-and-plate rheometry measurements in CTAT micellar solutions.¹⁴

Figure 11 depicts the apparent shear rate as a function of dimensionless time t/τ_d for different pressure gradients. For small ∇P such that $\dot{\gamma}_{app}$ is within the Newtonian flow regime (curve a), the steady state is reached very rapidly ($t/\tau_d < 1$). As the applied pressure gradient is increased, but still below the shear-banding region (curve b), the time required to achieve steady state increases, although it is still quite fast ($t/\tau_d \approx 1-5$). However, as soon as the ∇P yields stresses larger the critical value (curve c), oscillations appear which last many hundredths relaxation times. In some cases, our model predicts oscillations for very long times ($t/\tau_d > 1000$). When the applied pressure gradient is in the high-shear-rate branch, once again steady

conditions are reached quite quickly, although small oscillations are detected at short times.

Discussion and Conclusions

Based on the reptation theory of Doi–Edwards for polymer solutions, McLeish and Ball proposed that the reptation τ_{rep} and the Rouse τ_R characteristic times provide two conditions in the shear stress–shear rate relationship which give rise to the spurt effect.⁵⁰ However, these two characteristic times depend strongly on molecular weight ($\tau_{rep} \sim M^3$ and $\tau_R \sim M^2$), and so, molecular weight polydispersity, which is common in high molecular weight polymer solutions, masks the discontinuity in the σ – $\dot{\gamma}$ relationship.

Wormlike micellar solutions also exhibit a broad size distribution but because of the chain breaking and recombination processes that average the chain length distribution, these systems exhibit a narrow distribution of characteristic times in the fast breaking regime; that is, they behave as highly monodisperse systems.¹⁸ Hence, wormlike micellar solutions are excellent candidates to examine the spurt effect.

The phenomenological model used here was forwarded by us to mimic the nonlinear rheological behavior of wormlike micellar solutions in instantaneous stress relaxation, inception of shear flow, interrupted shear flow and other flow situations.²² Recently, we modified this model by introducing a shear rate-dependent kinetic constant for micelles breaking to predict the main features of shear-banding flow in cone-and-plate rheometry.¹⁴ This model has six parameters (φ_0 , φ_∞ , G_0 , λ , k_0 , and μ_1), whose values depend on surfactant concentration (Figure 1) and temperature.²² All the parameters are obtained from single and independent rheological experiments and with these values, other rheological data can be reproduced. The model predicts that the σ – $\dot{\gamma}$ relationship for micellar solutions has an inflection and the shape of a sigmoid with an unstable region between two critical shear rates (cf. Figures 2–4). The model besides, forecasting both the homogeneous and the nonhomogeneous flow regions, shows the existence of a low- and a high-shear-rate branches (Figure 3) and of a critical point where shear-banding flow vanishes. Both metastable branches and a critical point have been observed experimentally.^{20–25,40,41} The model also predicts the presence of oscillations and long transients associated with shear-banding flow in cone-and-plate rheometry.^{21,22}

An important question about shear-banding flow is how to set the position of the stress at which the system separates into bands? Recently, Olmsted and Lu⁴⁴ calculated phase diagrams for rigid-rod suspensions in shear flow solving the interfacial profile between phases (isotropic, nematic, and/or log-rolling) for the modified Doi–Edwards equation, and used its properties to determine the coexistence stress. Their criterion was the equality of the chemical potential of the bands. Our model, just like the modified Doi–Edwards' model, has three stable solutions in homogeneous planar shear flow. Here it is used together with the generalized Gibbs equation of viscoelastic fluids under shear flow⁴⁹ to derive a criterion for the coexistence of bands under shear flow. The criterion for bands coexistence is the equality of the extended Gibbs free energy of the bands. The predicted stress plateau coincides remarkably well with experimental data (Figure 4).

One of the parameters of the model (μ_1) is directly related to the shear-banding region. The model shows that the intensity of shear banding, which is the difference between the maximum and minimum values of stress in the instability region, increases as μ_1 increases (Figure 6). The shear-banding intensity parameter

also determines the time required to reach steady state after inception of shear flow. The magnitude of μ_1 is related to the width of the region where no steady state is reached (see Figure 6 of ref 14). Furthermore, the width and magnitude of the stress plateau also determines μ_1 .

In pipe flow, our model also captures the main features observed by NMR velocimetry such as distinct shear bands, one at the tube center and another near the pipe wall. The latter one, which supports a very high, approximately constant, shear rate next to wall, grows in thickness with increasing shear rate. Furthermore, our model reproduces qualitatively the experimental wall stress versus apparent shear rate for short residence times and once steady pipe flow is achieved, its predictions are quite accurate (Figure 8). As it was shown elsewhere,⁵² the appearance of shear banding depends on the residence time of the fluid in the pipe. If the residence time is short (small L/D), the data and the predictions approach that of a Newtonian behavior where no shear banding has occurred. As the residence time increases, shear banding develops and the plateau stress becomes apparent.

To demonstrate that the development of shear banding depends on both the stress level and residence time, it is useful to show that experimental data for short and long residence times in the pipe coincide with steady state data obtained by cone-and-plate rheometry (Figure 7). For short residence times ($L/D = 50$ or 100), capillary data overlap to those obtained in a cone and plate at the inception of flow or in stress ramps, where the stress increases linearly with time. Similarly, for long residence times ($L/D = 400$), the data overlap with those measured at simple steady shear flow in cone-and-plate geometry. Our model also reproduces these features (Figure 8). Moreover, even though our model over-predicts data for short L/D values (Figure 8), it demonstrates that the departures from steady data are more severe as L/D becomes smaller, just as it is observed in the experimental data.

Finally, our model also predicts that under certain values of pressure gradient or wall-shear rate, no steady state is ever reached (Figure 10) and that oscillations can remain for very long times (curve c in Figure 11). These results are consistent with the pressure drop variations observed when shear banding forms in pipe flow of CTAT micellar solutions (see Figure 10 of ref 52). In fact, these pressure drop variations do not seem to ever disappear. Also, for the pipe flow of a micellar solution of cetylpyridinium chloride/sodium salicylate (60 mM/100mM in water) a midflow region ($\dot{\gamma}_{\text{app}} = 7\text{--}20\text{ s}^{-1}$) has been reported where meaningful velocity data could not be recorded by NMR velocimetry, due to fluctuations in the velocity profiles.²⁴

In conclusion, we have presented here a simple model that predicts many features of the shear banding in steady shear and pipe flows. The model employs six parameters, all of which can be obtained from independent rheological experiments, and then they can be used to predict other rheological data.

Acknowledgment. This work was supported by The National Council of Science and Technology of Mexico (CONACYT grant 3343-P-E9607) and by CONACYT-ECOS (grant M96-E02).

References and Notes

- (1) Gravshold, S. J. *J. Colloid Interface Sci.* **1976**, *57*, 575.
- (2) Rehage, H.; Hoffmann, H. *Rheol. Acta* **1982**, *21*, 561.
- (3) Shikata, T.; Sakaiguchi, Y.; Urakami, H.; Tamura, A.; Hirata, H. *J. Colloid Interface Sci.* **1987**, *119*, 291.
- (4) Shikata, T.; Hirata, H.; Tocata, T. *Langmuir* **1987**, *3*, 1081.
- (5) Shikata, T.; Hirata, H.; Kotaka, T. *Langmuir* **1988**, *4*, 354.
- (6) Shikata, T.; Hirata, H.; Takatory, A.; Osaki, K. *J. Non-Newtonian Fluid Mech.* **1988**, *28*, 171.
- (7) Shikata, T.; Hirata, H. *Langmuir* **1989**, *5*, 348.
- (8) Rehage, H.; Hoffmann, H. *Mol. Phys.* **1991**, *74*, 933.
- (9) Rehage, H.; Hoffmann, H. *J. Phys. Chem.* **1988**, *92*, 4712.
- (10) Rauscher, A.; Rehage, H.; Hoffmann, H. *Prog. Colloid Polym. Sci.* **1991**, *84*, 99.
- (11) Kern, F.; Zana, R. S.; Candau, J. *Langmuir* **1991**, *7*, 1344.
- (12) Soltero, J. F. A.; Puig, J. E.; Manero, O.; Schulz, P. C. *Langmuir* **1995**, *11*, 3337.
- (13) Soltero, J. F. A.; Puig, J. E.; Manero, O. *Langmuir* **1996**, *12*, 2654.
- (14) Bautista, F.; Soltero, J. F. A.; Pérez-López, J. H.; Puig, J. E.; Manero, O. *J. Non-Newtonian Fluid Mech.* **2000**, *94*, 57.
- (15) Cates, M. E. *Europhys. Lett.* **1987**, *4*, 497.
- (16) Cates, M. E. *Macromolecules* **1987**, *20*, 2289.
- (17) Cates, M. E. *J. Phys. Fr.* **1988**, *49*, 1593.
- (18) Cates, M. E.; Candau, S. J. *J. Phys.: Condens. Matter* **1990**, *2*, 6869.
- (19) Turner, M. S.; Cates, M. E. *Langmuir* **1991**, *7*, 1590.
- (20) Spenley, N. A.; Cates, M. E.; McLeish, T. C. B. *Phys. Rev. Lett.* **1993**, *71*, 939.
- (21) Grand, C.; Arrault, J. M.; Cates, E. *J. Phys. II Fr.* **1997**, *6*, 551.
- (22) Soltero, J. F. A.; Bautista, F.; Puig, J. E.; Manero, O. *Langmuir* **1999**, *15*, 1604.
- (23) Callahan, P. T.; Cates, M. E.; Rofe, C. F.; Smelders, J. B. F. A. *J. Phys. II Fr.* **1996**, *6*, 375.
- (24) Mair, R. W.; Callaghan, P. T. *J. Rheol.* **1997**, *41*, 901.
- (25) Britton, M. M.; Mair, R. W.; Lambert, R. K.; Callaghan, P. T. *J. Rheol.* **1999**, *43*, 897.
- (26) Vinogradov, G. V. *Rheol. Acta* **1973**, *12*, 357.
- (27) Decruppe, J. P.; Cressely, R.; Makhloufi, R.; Cappelaere, E. *Colloid Polym. Sci.* **1995**, *273*, 346.
- (28) Makhloufi, R.; Decruppe, J. P.; Ait-Ali, A.; Cressely, R. *Europhys. Lett.* **1995**, *32*, 253.
- (29) Berret, J. F.; Roux, D. C.; Porte, G.; Lindner, P. *Europhys. Lett.* **1994**, *25*, 521.
- (30) Schmitt, V.; Lequeux, F.; Pousse, A.; Roux, D. *Langmuir* **1994**, *10*, 955.
- (31) Spenley, N. A.; Yuan, X. F.; Cates, M. E. *J. Phys. II Fr.* **1996**, *7*, 1071.
- (32) Greco, F.; Ball, R. C. *J. Non-Newtonian Fluid Mech.* **1997**, *69*, 195.
- (33) Español, P.; Yuan, X. F.; Ball, R. C. *J. Non-Newtonian Fluid Mech.* **1996**, *65*, 93.
- (34) Boger, D. V. *Annu. Rev. Fluid Mech.* **1987**, *19*, 157.
- (35) McKinley, G. H.; Raiford, W. P.; Brown, R. A.; Armstrong, R. C. *J. Fluid Mech.* **1991**, *223*, 411.
- (36) Larson, R. G. *Rheol. Acta* **1992**, *31*, 213.
- (37) Byars, J. A.; Oztekin, A.; Brown, R. A.; McKinley, G. H. *J. Fluid Mech.* **1994**, *271*, 173.
- (38) Berret, J. F.; Roux, D. C.; Porte, G. *J. Phys. II Fr.* **1994**, *4*, 1261.
- (39) Berret, J. F. *Langmuir* **1997**, *13*, 2227.
- (40) Berret, J. F.; Porte, G.; Decruppe, J. P. *Phys. Rev. E* **1997**, *55*, 1668.
- (41) Porte, G.; Berret, J. F.; Harden, J. L. *J. Phys. II Fr.* **1997**, *7*, 459.
- (42) Olmsted, P. D.; Lu, C.-Y. D. *Phys. Rev. E* **1997**, *56*, R55.
- (43) Berret, J. F.; Porte, G. *Phys. Rev. E* **1999**, *60*, 4268.
- (44) Olmsted, P. D.; Lu, C.-Y. D. *Phys. Rev. E* **1999**, *60*, 4397.
- (45) Hess, S. Z. *Phys. A* **1977**, *87A*, 273.
- (46) Bautista, F.; De Santos, J. M.; Puig, J. E.; Manero, O. *J. Non-Newtonian Fluid Mech.* **1999**, *80*, 93.
- (47) Rehage, H.; Hoffmann, H. *Rheol. Acta* **1988**, *92*, 4712.
- (48) Shikata, T.; Hirata, H.; Takatori, E.; Osaki, K. *J. Non-Newtonian Fluid Mech.* **1988**, *28*, 171.
- (49) Jou, D.; Casas-Vázquez, J.; Criado-Sancho, M. *Thermodynamics of Fluid Under Flow*; Springer-Verlag: Berlin, 2000.
- (50) McLeish, T. C. B.; Ball, R. C. *J. Polym. Sci., Polym. Phys. Ed.* **1986**, *24*, 1735.
- (51) Makhloufi, R.; Decruppe, J. P.; Ait-Ali, A.; Cressely, R. *Europhys. Lett.* **1995**, *32*, 253.
- (52) Hernández-Acosta, S.; González-Alvarez, A.; Manero, O.; Méndez-Sánchez, A. F.; Pérez-González, J.; De Vargas, L. *J. Non-Newtonian Fluid Mech.* **1999**, *85*, 229.